



UPPSALA
UNIVERSITET

UPTEC Q 23006

Examensarbete 30 hp

Juli 2023

Increased build rate by laser powder bed fusion of SSAB steel powder

Colin Daly

Civilingenjörsprogrammet i teknisk fysik med
materialvetenskap



UPPSALA
UNIVERSITET

Increased build rate by laser powder bed fusion of SSAB steel powder

Colin Daly

Abstract

SSAB has built a pilot gas atomization facility looking to expand their expertise of steel into the metal powder and additive manufacturing industry. Laser powder bed fusion is an additive manufacturing method that melts and fuse metal feedstock powder together layer by layer using a high intensity laser. The complex process requires optimization in order to be competitive. The process parameters laser power, scan speed, hatch distance and layer thickness largely govern the build rate and total production time. To increase the build rate, two iterations of test cubes with unique parameters sets were experimentally printed. Evaluation of relative density, porosity, microstructure, hardness and mechanical properties was performed. All results were compared to a reference parameter set previously studied. A candidate parameter set successfully increased the build rate by 116% while maintaining satisfactory material properties.

Teknisk-naturvetenskapliga fakulteten

Uppsala universitet, Utgivningsort Uppsala/Visby

Handledare: Ulrika Fager, Gunnar Broberg Ämnesgranskare: Urban Wiklund

Examinator: Lena Klintberg

Populärvetenskaplig sammanfattning

SSAB vill öka bygghastigheten på sin stålpulver 3D printer

SSAB är världsledande inom höghållfast stål och har nu börjat producera stålpulver för att bredda sin expertis och repertoar. Stålpulver har många användningsområden, men SSAB har siktet inställt på additiv tillverkning, också kallat 3D-printing. 3D-printing är intressant för det möjliggör tillvekningen utav komplexa geometrier som konventionella tillverkningsmetoder har svårt för. Samtidigt kan materialåtgången minskas då endast det material som behövs faktiskt förbrukas. 3D-objekten designas med hjälp av datorer och på så vis kan formen optimeras för att sedan enkelt delas med någon på andra sidan jorden.

För att 3D-printa metall pulver kan metoden laserpulverbäddsfusion (L-PBF) användas. Processen börjar med ett tunt lager av metallpulver som jämnt sprids ut på en byggplatta. Sedan riktar lasern mot pulvret och den höga energin från lasern smälter och binder samman metallpulvret för att bilda det första lagret av det önskade objektet. Byggplattan sänks sedan ned och ett nytt lager av metallpulver sprids ut över det tidigare lagret. Lasern riktar igen mot pulvret och smälter samman det nya lagret med det föregående. Denna process upprepas lager för lager tills hela 3D objektet är färdigt.

Genom att kontrollera byggparametrarna laserstyrka, skanningshastighet, skanningsbredd och lagertjocklek kan bygghastigheten och materialegenskaperna optimeras. Bygghastigheten påverkar den totala tiden det tar att bygga ett objekt. Teoretiskt sett kan bygghastigheten höjas obegränsat, men i praktiken innebär det att materialegenskaperna påverkas negativt. Detta projekt ämnar därför att öka bygghastigheten så mycket som möjligt jämfört med en referens medan godtagbara materialegenskaper bibehålls.

Projektet utförde iterativa experiment där testkuber printades med olika byggparametrar och sedan analyserades. Materialegenskaperna som utvärderades var relativ densitet, porers storlek och form, mikrostrukturen, hårdheten och de mekaniska egenskaperna från drag- och slagprov. Resultaten sammanställdes till ett processfönster som beskriver hur en relativ densitet över 99,95% uppnås, vilket anses vara gränsen för att materialet ska vara användbart. Den mest lovande uppsättningen av byggparametrar visade sig resultera i material med materialegenskaper som liknade referensen och som ökade bygghastigheten hela 116%.

Contents

1	Introduction	1
1.1	Background	1
1.2	Additive manufacturing	1
1.3	Goals and limitations	2
2	Theory	3
2.1	Laser powder bed fusion	3
2.1.1	Powder properties	3
2.1.2	Process parameters	4
2.1.3	Scanning strategy	6
2.1.4	Optimizing the build rate	7
2.2	Microstructure and defects of low alloyed steel in L-PBF	8
2.2.1	Porosity	9
2.2.2	Melt pool dynamics	10
2.2.3	Solidification and in situ heat treatment	12
2.2.4	Analysis	12
3	Method	14
3.1	Material and powder properties	14
3.2	Process parameters	14
3.2.1	Printing	14
3.3	Analysis	17
3.3.1	Sample preparation	17
3.3.2	Porosity analysis	18
3.3.3	Microstructure	18
3.3.4	Hardness	18
3.3.5	Mechanical testing	19
4	Results	20
4.1	Printing	20
4.2	Porosity	21
4.3	Microstructure	24
4.4	Hardness	26
4.5	Mechanical testing	28
5	Discussion	29
5.1	Future work	30
6	Conclusion	31
	Appendix	38

1 Introduction

1.1 Background

SSAB is a global steel company with a leading position in high-strength steels and related services. SSAB's vision "A stronger, lighter and more sustainable world" [1] aims to minimize material consumption by substituting present solutions with lighter and better adapted steel for its use. SSAB produce many different grades of steel to match market and customers demands. The fundamental product is plate and sheets of steel with varying thickness that customers then rework to a desired shape or product. SSAB is now looking to expand their expertise in high-strength steel into metal powder, primarily for additive manufacturing (AM).

A pilot gas atomization facility has recently been built for material development and production of metal powders. To fully understand the product in its intended area of use a laser powder bed fusion (L-PBF) printer has been acquired for prototype printing. It is essential that the entire production chain is studied to offer full services. This explains the core of this project; to develop and optimize how a metal powders shall be processed in a L-PBF machine to achieve desired results.

1.2 Additive manufacturing

Additive manufacturing, also known as 3D printing, is a rapidly growing field that builds objects layer-by-layer using computer assisted design (CAD) [2, 3]. It offers the advantage of creating intricate designs that are challenging to achieve through traditional methods like casting and machining [2, 4]. Compared to conventional manufacturing, AM has the potential to reduce material waste by utilizing only the necessary amount of material for each part. By optimizing designs and topology through CAD and finite element analysis (FEA) parts can be tailored to meet different performance requirements throughout the build while minimizing the global net-shape [5, 6].

In L-PBF metal powder is melted and fused together using a high-powered laser. The process requires careful tuning of all input parameters to achieve desired material properties [7]. Creating a stable meltpool is crucial to avoid pore formation and ensure proper fusion between layers [8]. Porosity is the most prevalent and detrimental issue in L-PBF, as it introduces stress concentrations that can lead to fatigue or crack initiation sites [5, 7, 9].

The main drawback of AM compared to conventional manufacturing is the time it takes to produce a single object [4]. Even though AM create near net-shape parts, depending on its size and complexity, the process take anywhere from several hours to days or even weeks. Furthermore the process inherently creates a rough surface which may require post-processing depending on its application. This makes additive manufacturing less practical for large-scale production of standardized parts and more suitable for producing small quantities of complex, customized parts [2].

1.3 Goals and limitations

The purpose of this project is to gain and provide a fundamental understanding of the L-PBF process using a steel feedstock powder. The goal is to identify parameter sets that increase the build rate while maintaining satisfactory material properties. This will involve conducting experiments using derived parameter sets and conducting a thorough analysis of the results. The evaluation will focus on comparing material properties, including porosity, microstructure, hardness and mechanical properties. All results will be compared to a reference sample printed with previously studied process parameters.

The limitations of this project is that only the key parameters laser power, scan speed, hatch distance and layer thickness will be altered. The analysis will primarily be performed on the bulk material properties. Material composition and powder properties will be kept constant throughout the experiments and are provided by SSAB.

2 Theory

2.1 Laser powder bed fusion

L-PBF uses a high powered laser beam to fuse thin layers of feedstock powder into a three dimensional (3D) object. The laser is guided by mirrors from above to selectively melt predefined areas of each layer directed by a adapted CAD. Once the laser finish melting a layer the initial build plate is lowered in preparation of a new powder layer. Each powder layer is deposited and evenly spread by a recoater mechanism. This cycle is repeated until the object is finished and consequently submerged in a bed of unfused powder. The unfused powder is ultimately removed and recycled for future projects. The entire process is conducted inside a enclosed build chamber with circulating protective gas to avoid oxidation and other impurities [5], and is demonstrated in Figure 1.

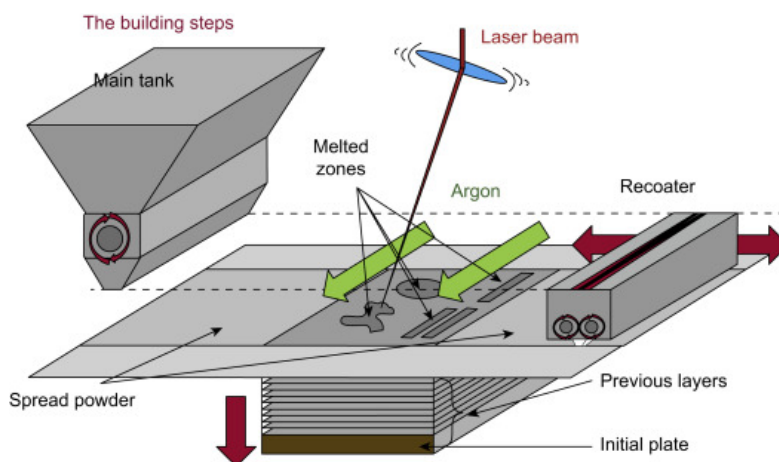


Figure 1: Illustration of the L-PBF process [10]. Argon gas is used as shielding gas in this illustration.

2.1.1 Powder properties

The size distribution and morphology of the feedstock powder affect the L-PBF process where sizes between 15-50 μm has been shown to be optimal [11]. Additionally the morphology should be as spherical as possible since it decreases friction between powder particles and improves the flowability of the powder, thus gas atomized powder is predominantly used [11, 12]. Flowability can be measured by a Hall flowmeter, where a specific weight of powder runs through a funnel following ISO 4490. High flowability is important to ensure that the recoater can feed and apply uniform powder layers [12].

The size distribution and morphology can be determined by image analysis of the powder following ISO 13322-2. The morphology is partially described by the average sphericity (SPHT) and aspect ratio (b/l), where b is breadth and l is

length [13]. Sphericity is defined in equation 1 below.

$$SPHT = 4\pi A/p^2 \quad (1)$$

where A and p represents the powder particles measured average area and circumference respectively [13]. The aspect ratio is defined in equation 2 below.

$$b/l = x_{cmin}/x_{Femax} \quad (2)$$

where x_{cmin} represents the shortest chord and x_{Femax} signifies the Feret diameter, the longest possible diameter [13].

The size distribution is described by the measurements d_{10} , d_{50} and d_{90} which are percentages describing the amount of particles smaller than a specific average diameter size. d_{50} thus defines the median particle size, d_{90} the size which 90% of the particles are smaller than and d_{10} the size which only 10% are smaller than, visible in Figure 2 [14, 15].

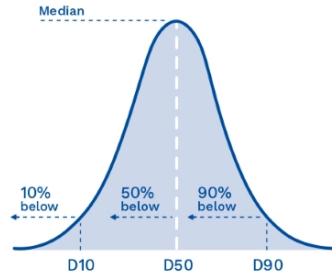


Figure 2: The size distribution describing particle size measurements d_{10} ($D10$), d_{50} ($D50$) and d_{90} ($D90$) [14].

2.1.2 Process parameters

The most influential parameters of the printing process, called the key parameters from now on, are laser power P (W), scan speed ν (mm/s), hatch spacing h (mm) and layer thickness t (mm) [16], seen in Figure 3. These key parameters largely govern the melt pool behaviour and progression through the process. To achieve fully dense objects the continuity of the melt pool is crucial and directly influence how the layers and melt tracks fuse together. The melt pool is required to have sufficient overlap between both layers and melt tracks as seen in Figure 3.

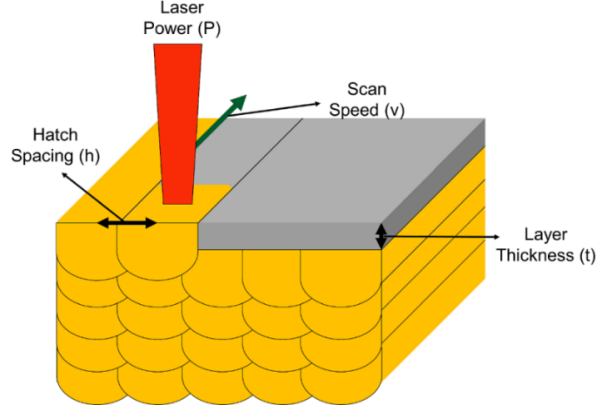


Figure 3: The figure shows a cross section of a build in progress where a powder layer is converted into a solid layer constituted of overlapping solidified melt pools [8].

Two expressions based on the key parameters are often discussed in literature, the build rate b and energy density E_d . The build rate is used to estimate the production time τ of a object with a specific volume V . It is defined in equation [3] as the product of the scan speed v , hatch spacing h and layer thickness t [17].

$$b = \frac{V}{\tau} = vht \quad [mm^3/s] \quad (3)$$

The energy density describes the thermal energy input per volume, which is often coupled to the resulting melt pool and material properties [17, 18]. The energy density should be moderate and tuned to the material, too high can cause excessive vaporization and too low will lead to insufficient fusion. It is defined in equation [4] as the laser power over the build rate [18].

$$E_d = \frac{P}{vht} \quad [J/mm^3] \quad (4)$$

To successfully operate the L-PBF process these key parameters must be tuned to find a operating window. A operating window is a theoretical range of parameter sets which yield desired material properties for a specific material. Figure [4] exemplifies how combinations of parameters can vary but still remain inside the operating window. During process development the operating window often aim to produce objects with a high relative density [7].

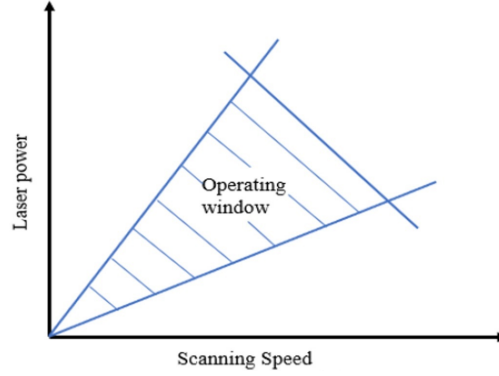


Figure 4: Example of a operating window of two input parameters; laser power and scan speed. Adapted from [7].

2.1.3 Scanning strategy

The scanning strategy decides what pattern is used when guiding the laser across the surface and is composed of straight scan vectors which is impactful for the final microstructure [18]. The simplest scan pattern is unidirectional scanning which uses parallel scan vectors seen in 5a. The bi-directional pattern is similar but alternates the direction of parallel scan vectors seen in 5b. The surface can be split up into smaller pieces called island patterns seen in 5c. Another common method is the stripe scan that follows overarching stripes with bi-directional scanning by the width of the stripe, called stripe length, seen in 5d [7, 8, 15].

Between each layer the scanning strategy usually includes a rotation of the pattern to mitigate anisotropic melting behaviour [18]. 67° is the most common rotation since it provides the greatest number of orientations before repeating the original scan orientation [19].

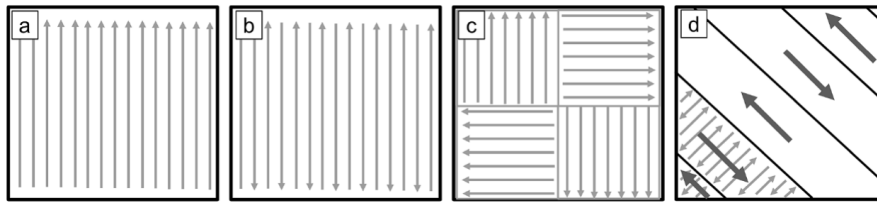


Figure 5: Examples of scan patterns; a) unidirectional, b) bi-directional, c) islands and d) stripes [8].

When building at an angle, special conditions are encountered where melting is done partially above only powder, referred to up-step and down-step [20]. To enable building complicated geometries hollow support structures are often added and the steps are done with specialized parameter sets. Contour scans around the outer perimeter of the build are commonly performed regardless to improve the surface roughness [8].

2.1.4 Optimizing the build rate

From a financial standpoint, a high build rate is always advantageous. Studying equation 3 the build rate can be increased indefinitely by increasing either the scan speed, hatch distance or layer thickness. However it can not be done carelessly as it simultaneously decreases the energy density if the laser power is not increased, following equation 4. Additionally to establish a operating window simply using the build rate or energy density can be deceptive since it fails to describe how the inputted energy affects the melt pool. In Figure 6 Scipioni et al. [21] prove that retaining a constant energy density is not sufficient to maintain stable melt tracks.

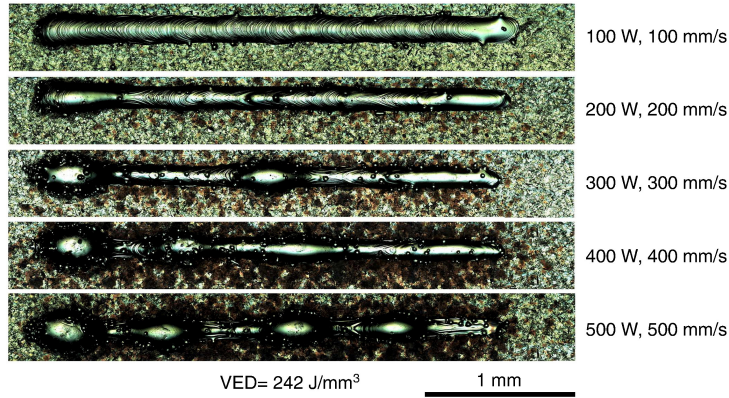


Figure 6: Single melt track experiment using a constant energy density (VED in the Figure) when varying the laser power and scan speed [21].

Figure 6 show how the increasing laser power and scan speed disrupts the stability of the melt pool instigating critical flaws. Eventually the operating window is exceeded and the resulting material properties will deteriorate, often being a trade-off between build rate and surface quality [7]. Optimization of the build rate is therefore done within the operating window while considering the energy density.

Yiu et al. [22] instead only varied the scan speed and hatch spacing while maintaining a constant energy density yielding successful results. Compared to the provided reference data both laser power and layer thickness had been increased justifying many possibilities to increase the build rate.

The build rate in equation 3, $b = \nu ht$, only consider the exposure time of the laser while printing, thus neglecting the recoating time and consequentially underestimating the production time. The recoating time is problematic to improve since its precision is fundamental for the process. It is however possible to reduce the number of recoating cycles by increasing the layer thickness, implying that layer thickness is preferential to scan speed and hatch spacing when increasing the build rate [17]. Schwerz et al. proposes a expanded expression for the build rate, equation 5, that consider both the recoating time τ_{tr} and, a design parameter, the

average build area utilization R [17].

$$b = \frac{V}{\tau} = \frac{Rvht}{R + vh\tau_{tr}} \quad [mm^3/s] \quad (5)$$

Wang et al. [23] and Shi et al. [24] both attempted to dramatically increase the layer thickness, several times thicker than the reference. They used a pulsed laser source instead of a continuous, but successfully managed to produce material with high relative density, using a relatively high laser power though still a low energy density. Sheuan Jason Ten et al. [25] also showed promising results of increasing the build rate while balancing the energy density by increasing the laser power.

2.2 Microstructure and defects of low alloyed steel in L-PBF

The layer-by-layer construction of L-PBF inadvertently leads to remelting and reheating of the previously printed layers. The different layers and parallel melt tracks form a curtain type pattern throughout the solidified material generated by the heat affected zone (HAZ) beneath each melt pool visible in Figure 7 [11]. The pattern naturally follows the build direction asserting an anisotropic behaviour unlike any other production method, and are visible due to crystallographic changes in the microstructure from the in situ heat treatment.

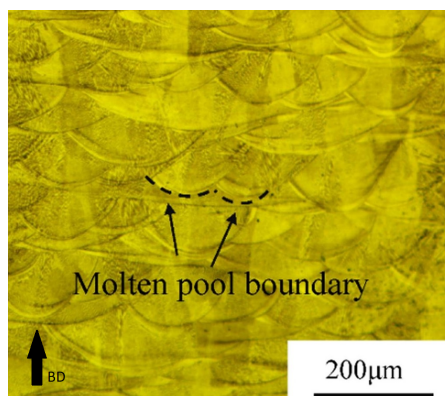


Figure 7: Typical curtain like behaviour of the resulting microstructure following a L-PBF process. The build direction BD is shown in the bottom left [19].

There are two stable melt modes in L-PBF, the conductive- and keyhole mode, with a unstable transition mode between them seen in Figure 8 [7]. During conductive mode the melt pool is shallow and proportional to its width [26]. In keyhole mode the depth of the melt pool is elongated due to a higher energy input that vaporise some of the metal. The vaporisation creates a recoil pressure that maintains a keyhole below the laser beam, as seen in Figure 8 [26].

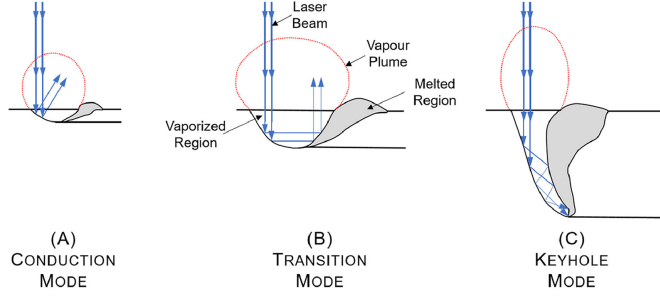


Figure 8: Melt pool in (A) conduction-, (B) transition- and (C) keyhole mode [26].

2.2.1 Porosity

The primary defect of L-PBF is pores in the finished object induced by the complex layer by layer production. Pores generate stress concentrations that act as crack-initiation and propagation sites and thus have a negative influence of material properties [27]. Therefore porosity measurement often serve as a fundamental criterion when developing process parameters [5, 8]. Porosity is measured using relative density, either by Archimedes principle or by image analysis of a surface. A recurring threshold of an acceptable relative density is 99.95% [16]. There are three main types of porosity; lack of fusion-, keyhole- and entrapped gas pores [8].

Lack of fusion occur when there is incomplete melting and fusing between adjacent powder particles and underlying surface. Lack of fusion pores often manifest either between scan tracks, inter-track, or layers, inter-layer, and are characterized by their irregular shape exemplified in Figure 9 [8, 28].

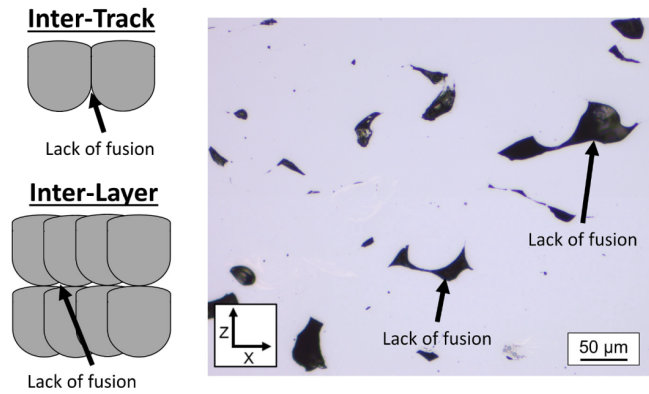


Figure 9: Example of lack of fusion pores and where they predominantly occur, either inter-track or inter-layer [8].

keyhole pores are created when the keyhole collapses during keyhole mode, called keyhole depression seen in Figure 10 [29]. This happens when the vapor recoil pressure is insufficient or too unstable to maintain the keyhole. Consequently residual vapor is trapped at the bottom of the melt pool without time to reach the

surface. The keyhole pores tend to have a partially spherical shape, albeit with slight irregularities due to their volatile creation [30, 31].

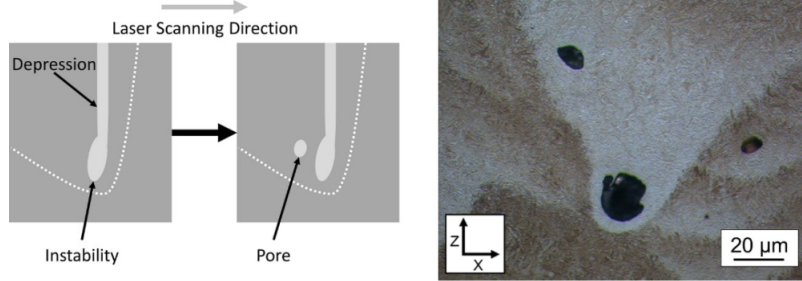


Figure 10: Visualisation of how a keyhole collapses due to an instability thus creating a keyhole at the bottom of the melt pool, combined with a physical representation to the right [8].

Entrapped gas pores are small spherical pores, seen in Figure 11a, that essentially are always present during L-PBF [22]. They form when gas or vapor get trapped within the melt pool during the printing process, similar to the keyhole pores. However gas pores are smaller relative to lack of fusion- and keyhole pores and mainly dependent on material and powder properties rather than process parameters. They can form due to vaporization of low melting point constituents of the alloy, from voids in the powder bed due to poor stacking or porosity of the feed powder itself. The two latter are illustrated in Figure 11b. Spherical pores are preferential to irregularly shaped ones since they better maintain structural integrity [5, 27].

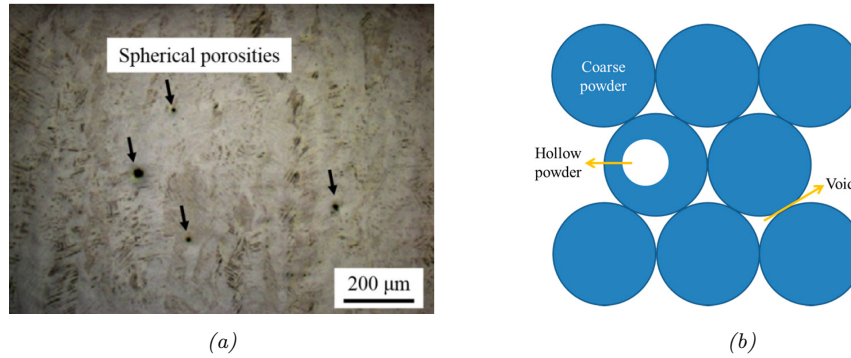


Figure 11: (a) shows gas pores spread out in the bulk of L-PBF printed sample [32]. (b) shows how the powder properties can transfer voids and pores from the powder bed to the melt pool [23].

2.2.2 Meltpool dynamics

When the laser beam hits the powder bed it is absorbed by the powder particles and underlying surface. The absorbed energy heats the material until melting within milliseconds thus creating a melt pool. The size, shape and stability of the

melt pool is a result of the chosen process parameters. If the laser is too intense it can cause excessive vaporization of the material that create a recoil pressure.

The recoil pressure can cause hot spatter which is an ejection of particles from the melt pool, illustrated in Figure 12(b). There is also cold spatter driven by the significant pressure drop surrounding the incident laser that cause a upwards gas flow [33]. These spatter particles are often agglomerated powder lumps that inevitably will settle somewhere on the nearby powder bed which can interfere with the subsequent layers by requiring more energy to remelt causing lack of fusion pores [34].

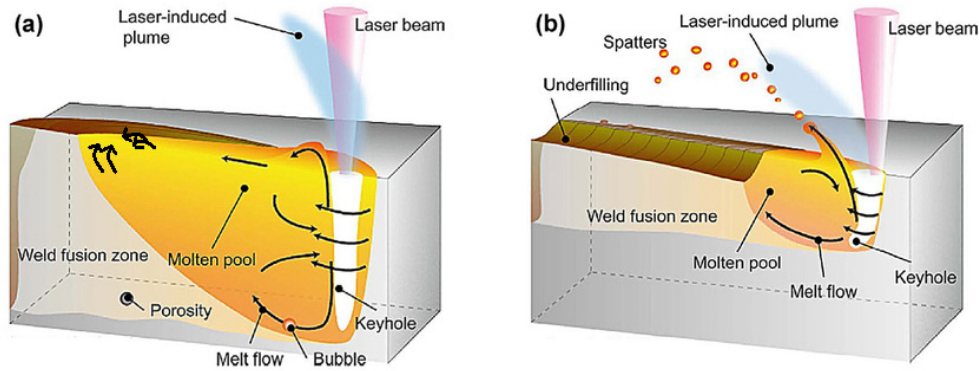


Figure 12: Figure presenting different heat transfer phenomena present in the melt pool. The arrows surrounding the keyhole show the Marangoni flow. In (a) the Plateau-Rayleigh phenomena is illustrated with the arrows at the surface end of the melt pool. In (b) hot spatter is visible being ejected from the melt pool due to the laser induced recoil pressure. Adapted from [35]

The melt pool experiences complex heat transfer phenomena before solidifying seen in Figure 12 [36]. The laser beam creates a significant temperature gradient between the center of the melt pool and its edges. This temperature gradient cause a Marangoni flow, a convection driven fluid motion, that attempt to balance the different surface tensions within the melt pool [19], visible around the keyhole in Figure 12.

Additionally the Plateau-Rayleigh instability is visible at the end of the melt pool in Figure 12(a). This is a phenomena driven by the liquids surface tension's will to minimize its surface area into spheres and becomes noticeable when the width to length ratio of the melt pool reaches a critical point. Combined with insufficient wetting of the underlying surface this is the main cause of balling [37].

Balling is the result of a unstable melt pool which break up melt tracks into balls. These irregularly shaped balls can further hinder the process by interfering with the recoater and remelting [21, 37]. As successive layers are added, the problem expands upon itself, aggravating its impact and damaging the relative density [19]. In Figure 13 Ahmed et al. [7] suggest that balling, keyhole- and lack of fusion pores are the primary defects when developing a operating window.

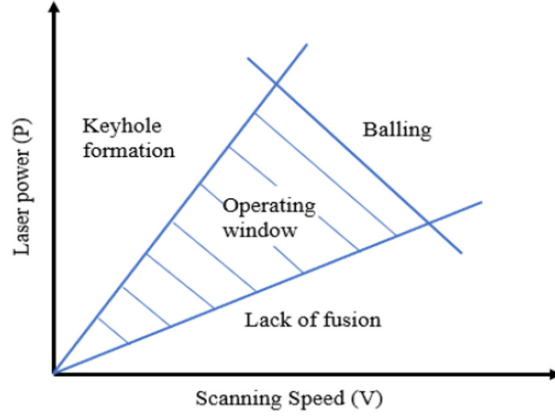


Figure 13: Operation window encapsulated by different defect phenomena [7].

2.2.3 Solidification and in situ heat treatment

As low alloy steel solidifies primarily γ phase austenite will form. Depending on the cooling rate it can then undergo different solid state transitions to various other phases. During L-PBF extremely high cooling rates between 10^4 and 10^6 K/s are experienced causing a rapid phase transformation into martensite [29]. This diffusionless transition traps carbon atoms in the structure, leading to the hard and brittle martensitic microstructure with high internal stresses. The extent of martensite formation depend on the chemical composition and significantly impact the mechanical properties of the printed object, such as its hardness, strength and toughness.

The solid state phase changes are driven by the reheating of previous layers which allow diffusion to occur. This reheating process can be regarded as a type of annealing or tempering, serving to alleviate internal stresses [38]. Nevertheless, the repetitive thermal gradients resulting from this process may induce thermal stresses, leading to warping and curling of the object [39]. To lower the thermal gradients build plate preheating is often utilised which help mitigate the consequences and also aid with the adhesion of the first layers.

2.2.4 Analysis

The microstructure can be studied using light optical microscopy (LOM) and scanning electron microscopy (SEM) among others. A SEM can provide high-resolution imaging and detailed analysis of surface morphology, elemental composition, and crystallographic information [40]. Energy dispersive X-ray spectroscopy (EDS) is used for chemical analysis of surfaces. Electron backscatter diffraction (EBSD) can provide information of defects, plastic deformation, misorientation, grain size, and crystallographic texture.

In EBSD, the electron beam is scanned across the surface of a tilted crystalline sample. The diffracted electrons at each point form a Kikuchi pattern that can

be detected and analysed using dedicated hardware and software. By indexing each point, phase and crystallographic orientation information is obtained, from which the microstructure can effectively be reconstructed [41]. The hit rate, i.e. the fraction of points that can be successfully indexed, of EBSD is considered acceptable above 90% and depend on the sample preparation and operation of the machine. Computation and analysis can deduce data missing due to the hit rate to a some extent. In general, when examining the martensitic BCT structure, the EBSD detector tends to interpret the observed Kikuchi pattern as a BCC structure with low band contrast because the structures are so similar and BCC is more common.

Hardness and mechanical properties also provide necessary information of the microstructure. Hardness measurements are presented as follows: achieved hardness, hardness scale, applied load (kg) and time of applied load (seconds), ex. 410HV5/10. Mechanical properties are measured by tensile and impact testing. Tensile tests determine the yield strength $R_{p0.2}$ (Pa), tensile strength R_m (Pa) and the ultimate elongation before breaking A_5 (%) [42]. Impact testing is performed by allowing a pendulum to swing through a sample and measuring the amount of energy lost from the impact (J) [43].

3 Method

3.1 Material and powder properties

The provided metal powder was SSAB AM TS1. Chemical composition as well as size and morphology data was provided by SSAB. Table 1 presents the chemical composition and Table 2 presents the powder properties of the powder used in the study. The size and shape analysis was performed according to ISO 13322-2.

Table 1: Chemical composition in wt-% of the provided TS1 steel powder used in the experiments.

	C	Si	Mn	Cr	Mo	Fe & other
SSAB AM TS1	0,22	1,1	0,8	1,05	0,2	bal.

Table 2: Particle size and shape characteristics of the provided TS1 powder used in the experiments.

d ₁₀	d ₅₀	d ₉₀	SPHT	b/l
24 μm	33 μm	44 μm	0.91	0.88

3.2 Process parameters

3.2.1 Printing

Printing was performed using an SLM280 machine equipped with a 400W Yb-fiber laser source. Three experimental runs were carried out, involving two optimization runs for parameter sets and one for evaluating mechanical properties. In each build, the same powder type, SSAB AM TS1, was used. Argon served as the shielding gas, and a stripes scanning pattern was employed. Additionally, a build plate preheating of 100°C was applied. All builds were prepared using Materialise Magics v.25 software.

During each of the first two iterations, eighteen 25 mm cubes with unique parameter sets were printed for analysis. These cubes were arranged in a shifted matrix pattern, as shown in Figure 14. Each cube was labeled according to the print iteration (n) and its position on the build plate (m), resulting in designations such as n.m. The reference parameter set, 1.1, was used as a benchmark to standardize and compare all other parameter sets. Note that from this point onward, most parameters presented are normalised values to the 1.1 parameter set.

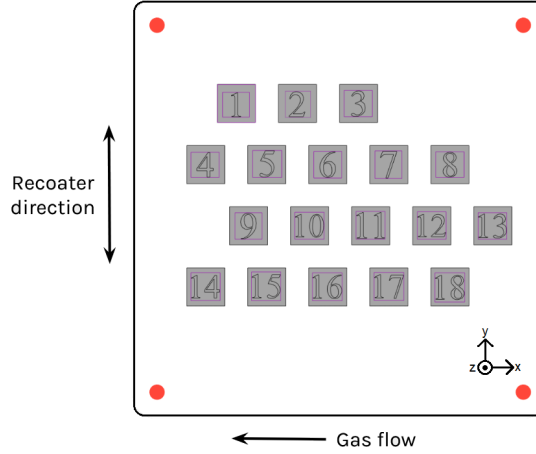


Figure 14: Layout of test cubes on the build plate.

The parameter sets of the 1st iteration was based of a initial literature review [4, 7, 15, 16, 17, 19, 21, 22, 23, 24, 25, 27, 28, 44], and ultimately focused on improving the layer thickness while maintaining a stable E_d . Three sub sets of incremental layer thicknesses were selected where the laser power and scan speed balance the build rate and energy density equally to compose comparable trends between the sub sets, visible in Figure 15. All data is normalised to the reference parameters and is presented in the Appendix Table 6.

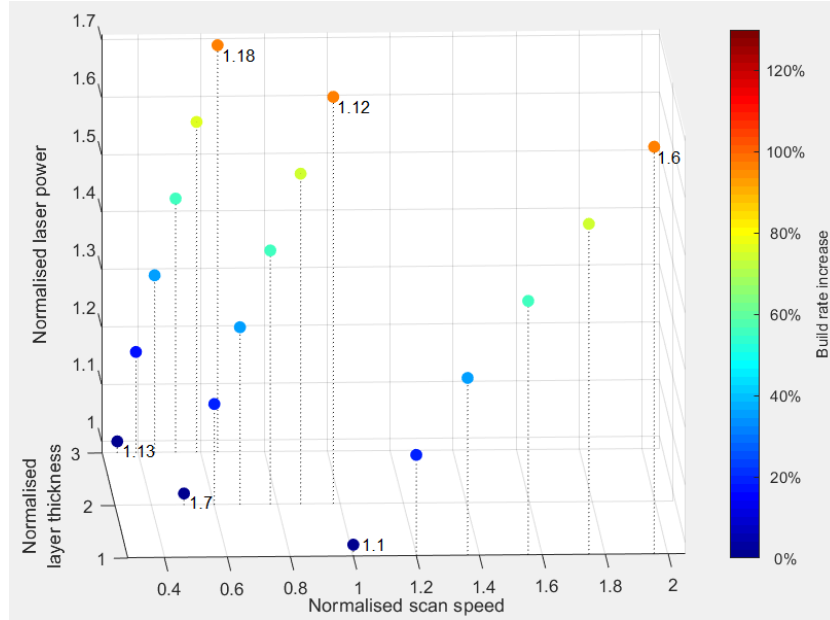


Figure 15: Visual representation of selected parameter sets during the 1st iteration of printing. As the layer thickness increases laser power and scan speed balance this to create comparable ranges of build rate increase (normalised numbers). Hatch distance is kept constant and identical to that for cube 1.1. The beginning and end of each range is labeled.

The 2nd iteration was created after the porosity analysis and evaluation of the 1st iteration. The most promising parameter set of the 1st iteration and one that doubled the layer thickness of the reference, was used as a origin point for developing a operating window. New parameter sets were chosen in a grid pattern, seen in Figure 16, to encapsulate the chosen parameter set while maintaining a constant layer thickness. All data is normalised to the reference parameters and is presented in the Appendix Table 7.

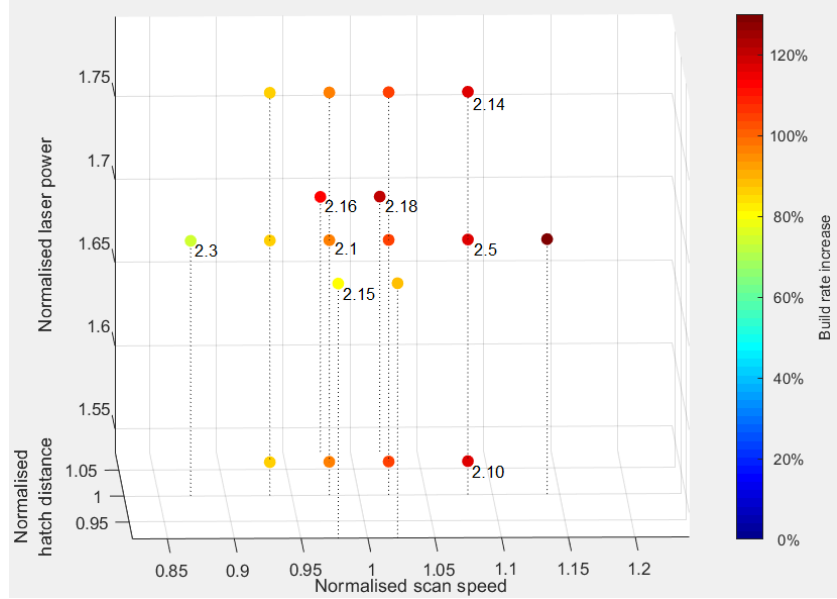


Figure 16: Visual representation of selected parameter sets during the 2nd iteration of printing. Layer thickness is kept constant and identical to that for cube 1.1. Cubes selected for further analysis are labeled.

The 3rd printing utilized the two most promising parameter sets from the 2nd iteration when producing cylindrical and square rods for mechanical testing. The test rods were printed with different orientations relative the build plate , standing and lying, and thus with different test plane directions, XY and XZ, as seen in Figure 17b. The two parameter sets were chosen after porosity, hardness and microstructure analyses were completed and evaluated. Each test rod was printed in six copies.

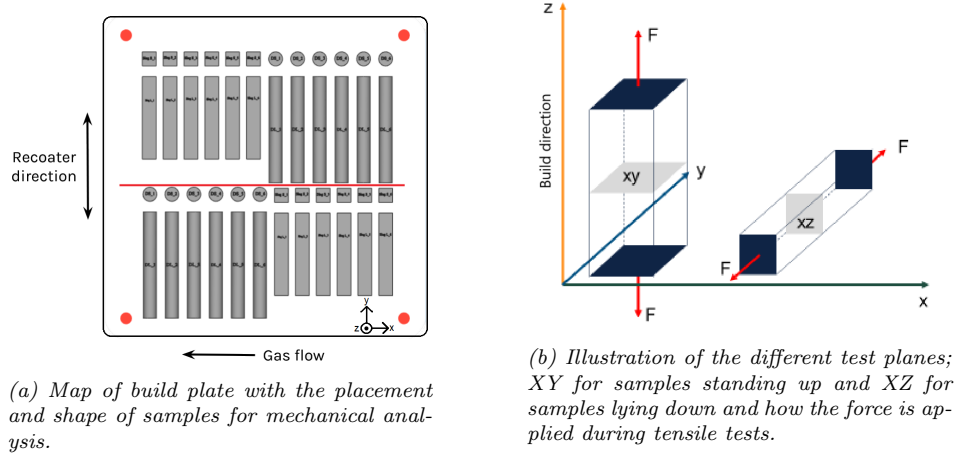


Figure 17: Layout of the 3rd printing.

3.3 Analysis

3.3.1 Sample preparation

The printed cubes were removed from the build plate using a metal saw and then precisely sectioned using a Struers secotom 60 in the XZ plane, seen in Figure 17b, to expose the bulk along the build direction. The cut was performed in ExciCut mode at 0.1mm/s and 1200 rpm [45]. Next the sectioned cubes were mounted in polyfast by a Struers citopress 20 after making sure to mark the build direction. The settings were a temperature of 180°C and a pressure of 250 bar. After this grinding and polishing was performed using a Struers tegramin 30, progressively using finer cloths combined with suitable lubricant and abrasive particles. Between each step the samples were cleaned with ethanol, wiped with cotton and dried.

Depending on the intended analysis method the grinding and polishing steps were tailored. Samples analysed in LOM used piano 220 with water as lubricant for grinding. The polishing steps used MD-Allegro, MD-Dac and MD-Nep cloths in succession with accompanying lubricant containing abrasive particles of sizes 9, 3 and 1µm separately. Samples were then etched using nital 2% to expose the microstructure.

Samples studied in the SEM required more delicate sample preparation to avoid affecting the underlying surface. Grinding was done using SiC papers which were attached using a gekko-cloth and lubricated with water. Each grade of paper (500, 1200, 2000, and 4000) was sequentially used three times, with the paper being replaced after each use to ensure optimal results. The polishing was done using the same steps as for LOM samples, but with a additional MD-Nap cloth combined with abrasive particles of 1/4µm. To prepare the sample for EBSD a final oxide polish was performed using the etchant OP-U NonDry on a special Chem-cloth [45].

3.3.2 Porosity analysis

An overview picture of the exposed surface was stitched together composing of photos taken at 50x magnification in LOM. The overview picture was analysed using ImageJ 1.8.0 to determine the amount, size and shape of dark areas. The porosity is calculated as a area percentage of dark areas on the analysed surface, assuming all dark areas are pores. The grey scale threshold, which determines what degree of anomaly will register as impurity, was automatically adjusted by the software.

The area of each pore is calculated by the number of pixels it covers. The height and width of each pore is used to determine the average diameter and the circularity of the pore, the latter being a ratio between these measurement. The average diameter was then used to calculate the average equivalent circular diameter (ECD), which approximates each pore as a perfect circle and allows comparisons between pore populations.

Porosity analysis was also performed in the SEM utilizing the AZtecFeature version 6.0 SP2 software that perform EDS to distinguish pores from inclusions and other impurities after localizing them with the backscatter detector. The SEM porosity analysis was done covering a roughly 60% smaller area than the LOM analysis since the resolution is much higher and the process requires longer time. Impurities were analysed and sorted, leaving only true pores for the porosity analysis. Three samples were selected for SEM analysis after evaluating the LOM porosity analysis.

3.3.3 Microstructure

The microstructure was studied at high resolution with LOM and SEM. An assortment of samples was studied in LOM to find and observe trends when individual parameters changed. The top layer, which has a pristine microstructure without influence of additional powder or scanning on top, was examined to understand the melt pool behavior. Measurements and photographs in the LOM was taken using the software OLYMPUS stream essentials. In the SEM, EBSD was performed on one sample after the SEM porosity analysis. Three runs each were performed in the bulk and the top layer respectively.

3.3.4 Hardness

Hardness measurements were performed on a assortment of samples with a Qness Q30 A+ following ISO 6507. Samples were mounted into the machine and using the Qpix software a custom surface- and bulk profile was initiated seen in Figure 18. The hardness was measured in Vickers (HV), which uses a pyramidal indenter. Before starting a run each indentation site was checked to avoid hitting pores or other impurities.



Figure 18: Layout of hardness measurements which were compiled in two profiles: red for bulk and green for surface. Circled area of expected damage from the indentation is marked. The surface edge is visible at the top in grey, build direction (BD) is given.

The bulk profile, red in Figure 18, used 5kg load with 1mm steps on a straight line along the build direction. The surface profile, green in Figure 18, used a lower load of 0,3kg to approach the surface without affecting the results. It also used a zigzag pattern to avoid affecting neighboring indentations.

3.3.5 Mechanical testing

In total 48 sample rods were printed and prepared for mechanical testing as seen in Figure 17, using two selected parameter set. The cylindrical rods were machined into a samples for tensile testing according to ISO 6892-1. The square rods were prepared for impact testing, according to ISO 148-1, as charpy-V specimens with a notch on the opposite side of the intended striking surface to serve as a crack initiation site. The tests were performed in room temperature.

4 Results

4.1 Printing

During the 1st iteration of printing nine cubes, seen in Figure 19a, were stopped early in the process due to visible intense spatter. This was done to mitigate machine errors and make sure that other nearby cubes were not affected. During the 2nd iteration the process stopped midway due to a powder feeding error. The cubes were finished to about half their intended height and were deemed sufficient to perform a fair analysis. Further cube 2.17 was stopped early, however this was caused by human error when inputting parameters. Cubes that were stopped are assumed to be outside the operation window.

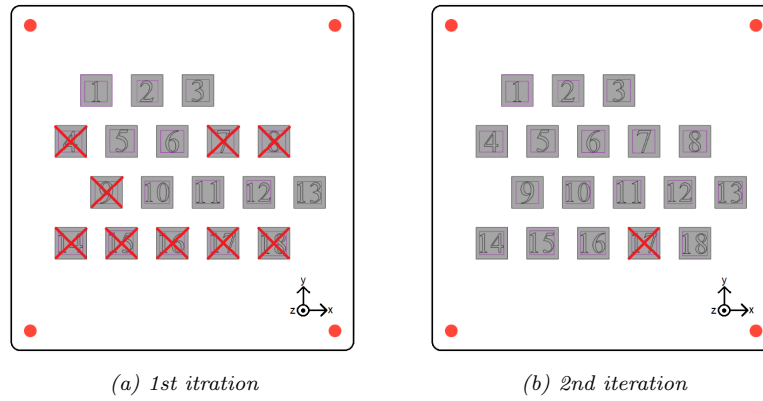


Figure 19: Overview of the cubes that were stopped during the first two iterations of printing. Cubes crossed with a red X were stopped, most often due to visible intense spatter.

Figure 20 shows that all cubes that finished printing either increased or matched the build rate of the reference cube 1.1.

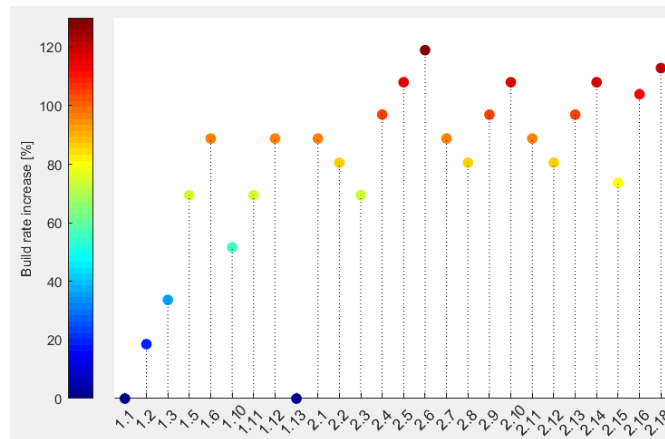


Figure 20: Graph showing the increased build rate of each successfully printed sample.

4.2 Porosity

1st iteration

In figure 21 some of the finished and analysed cubes from the 1st iteration are presented. The pictures are taken in LOM and were used for the porosity analysis presented in Figure 22. Cube 1.1 is the reference sample displaying little to no pores. Cubes 1.6 and 1.13 exhibit excessive keyhole and lack of fusion porosity respectively. Cubes 1.3, 1.10 and 1.12 have less porosities but is harder to analyse visually.

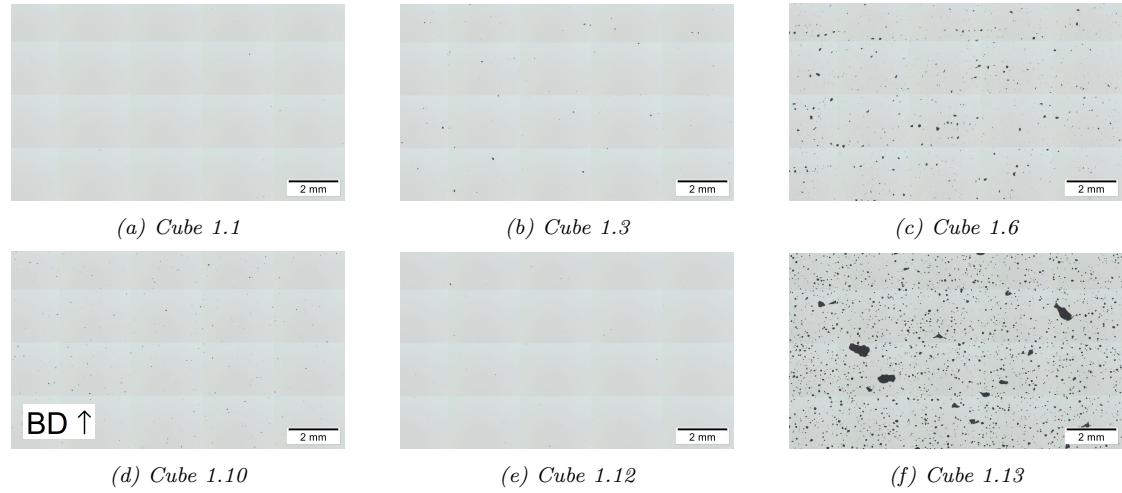


Figure 21: LOM images of polished samples from the 1st iteration cubes used for the porosity analysis. The build direction (BD), indicated in (d), is the same for all samples.

Figure 21 and 22 clearly show that among the six cubes shown, cube 1.13 has the lowest relative density and largest pores, which the ECD confirms. It is the only cube that tripled the layer thickness compared to the reference and finished printing, yet without increasing the build rate as seen in Figure 15 and 20.

In Figure 21 and 22, the reference cube 1.1 achieved the highest relative density and lowest ECD. The cubes 1.1-1.6 share the same layer thickness and exhibit a successive deterioration in performance as the laser power increases. This is evident from the growing presence of keyhole porosities observed across the samples. Cubes 1.10-1.12 alternatively show a positive trend as the laser power increases where keyhole pores diminish culminating in the successful parameter set used for cube 1.12 that nearly match the reference cube 1.1.

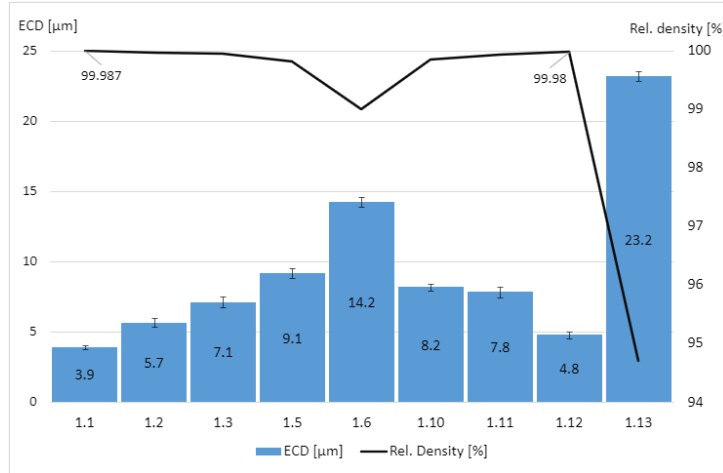


Figure 22: Results of the porosity analysis from the printable cubes of the 1st iteration.

2nd iteration

The 2nd iteration was stopped early due to a powder feeding error, see section 4.1, resulting in a smaller surface to analyse. This is visible in Figure 23 as the length scale differs from that in Figure 21 and the mounting resin is visible as dark areas around some edges, however the magnification and resolution is the same. All surfaces presented in Figure 23 show low porosity and are tough to visually separate from each other. Porosity image analysis was done for all finished cubes and are presented in figure 24.

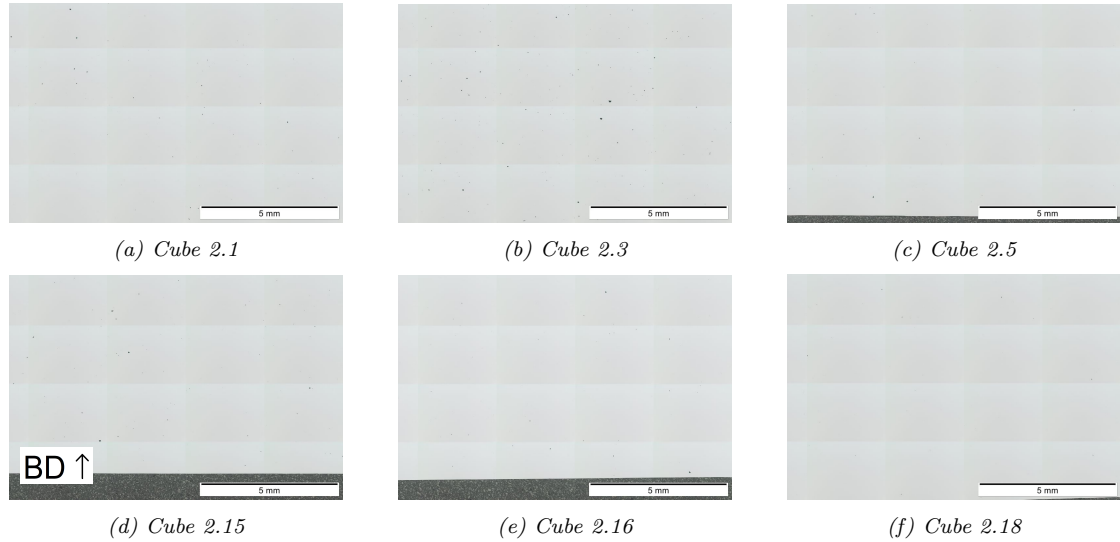


Figure 23: Polished samples from the 2nd iteration cubes studied in LOM. The build direction (BD), indicated in (d), is the same for all samples.

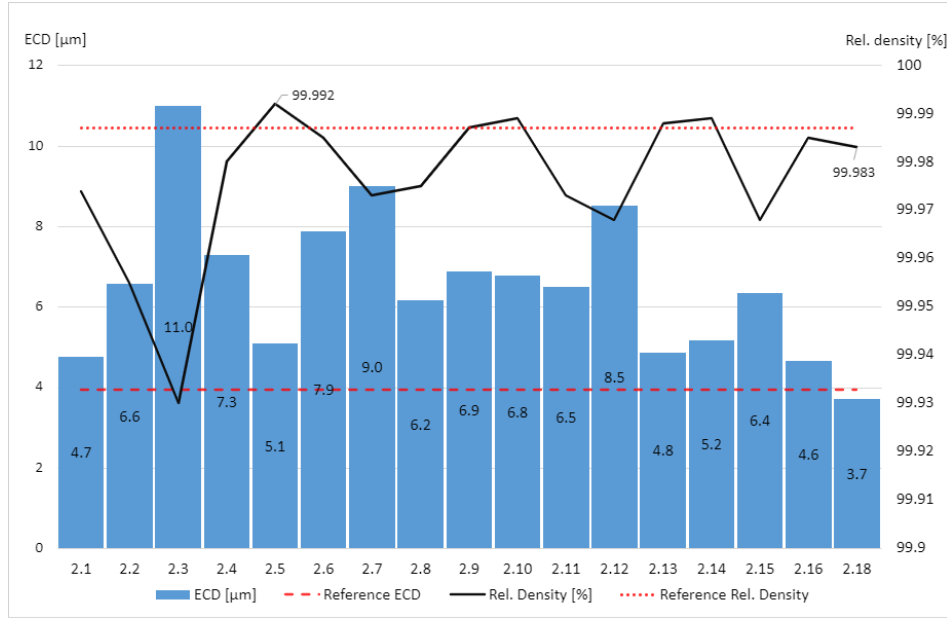


Figure 24: Results of the porosity analysis from the printable cubes of the 2nd iteration. The red dotted lines shows the result of the reference 1.1.

Studying Figure 23 and 24, cube 2.3 is the only cube with a relative density lower than the tolerable 99.95% threshold. Cubes 2.5, 2.9, 2.10, 2.13 and 2.14 acquired a similar or higher relative density than the reference cube 1.1, but simultaneously had a larger ECD. The only sample with a ECD lower than cube 1.1 was cube 2.18. The highest relative density of 99.992% was achieved by parameter set 2.5.

SEM analysis

Porosity analysis in the SEM was done for cubes 2.5, 2.16 and 2.18, which required new sample preparation. In figure 25a a overview of a analysed area for cube 2.5 is shown. All anomalies were chemically interpreted by EDS thus ensuring a more accurate pore analysis. The results are presented in Figure 25b.

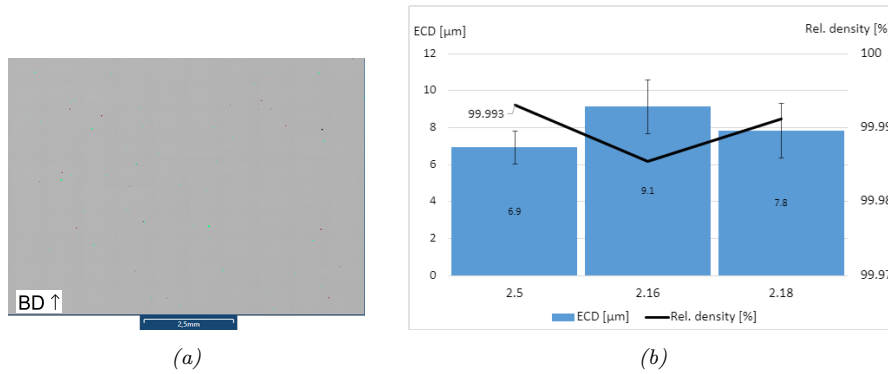


Figure 25: Overview image of cube 2.5 (a), and results from porosity analysis (b) performed in the SEM.

Figure 25b confirms the high relative density of the samples provided in Figure 23. The ECD increases for all samples and unlike the results from the LOM analysis cube 2.5 has a lower ECD than cube 2.18.

4.3 Microstructure

LOM

The microstructure of the top layers are presented for nine different samples in Figure 26. All samples show the resulting hardness indentations from the surface hardness profile test done prior to the microstructure analysis. The brighter area at the top is the result of the last layer solidifying into pristine martensitic structure. The underlying bulk layers have experienced a heat treatment altering its microstructure and appearance. Color gradient differences of samples is mainly due to handling error, software management and etching execution.

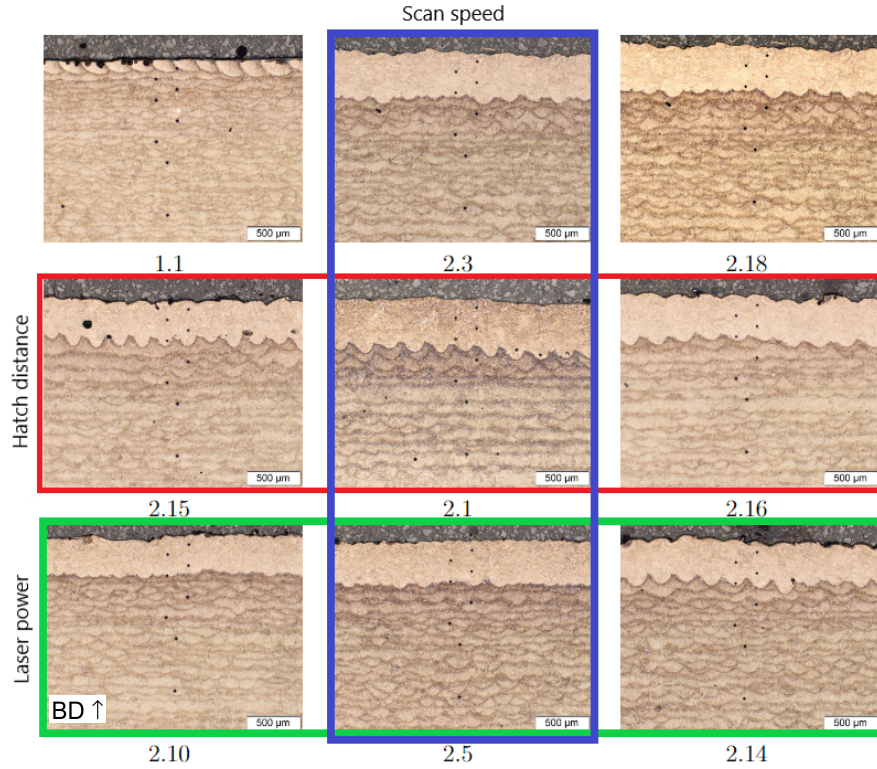


Figure 26: Overview images of the top layer and bulk taken in LOM. Moving downwards in the second column, marked in blue, the scan speed increases. Similarly the hatch distance increases when moving to the right in the second row (marked red) as does the laser power in row three marked green. The build direction (BD) is uniform for all samples. Note that the black spots at the surface of cube 1.1 is ethanol remnants.

Studying Figure 26 it is clear that differentiating the bulk microstructure of the different samples is difficult. However it is apparent that the microstructure of the

top layer differs between the reference cube 1.1 and the others. This is partially due to the 2nd iteration printing stopping early, causing it to skip the contour scan of the surface that cube 1.1 received. The contour scan employs unique parameter sets that render any meaningful comparisons futile. For all other cubes, considering the similar thickness of the top layer and the presence of visible keyhole pores at the bottom of the top layer in cubes 2.1, 2.14, and 2.15, it is likely that all cubes from the 2nd iteration were printed in keyhole mode.

Furthermore Figure 26 illustrates sub sets of individually increasing parameters also demonstrated in Figure 16. Scan speed increases from the top down in column two. Hatch distance and laser power increases from left to right in row two and three. Solely studying the top pristine martensitic layer, average measurements of the HAZ surrounding individual solidified melt pools were taken and are presented in Table 3. The depth represents the thickness of the top layer. The width is measured at the cubes top surface by studying grain boundaries from the solidification. The measurements have a high uncertainty due to heavily relying on human assessment.

Table 3: Measurements of the top layer from the three sub sets presented in Figure 26. Data is presented according to the example given in the top left corner. All measurements are in μm , the standard deviation is given following the \pm .

Sample	Depth	2.3	512 \pm 24		
	Width		331 \pm 14		
2.15	419 \pm 16	2.1	407 \pm 16	2.16	384 \pm 12
	220 \pm 13		277 \pm 7		252 \pm 8
2.10	383 \pm 11	2.5	389 \pm 12	2.14	410 \pm 14
	257 \pm 14		262 \pm 6		231 \pm 7

Table 3 show coherent trends of how the size and shape of the HAZ from the melt pool depend on the energy density. In column four the scan speed increases incrementally downwards in the table, thus decreasing the energy density which results in a shallower HAZ. The same result is visible in row two as the hatch distance increases from left to right. As the laser power increases from left to right in row three, there is a corresponding increase in the energy density, which leads to a deeper HAZ.

SEM

An overview EBSD inverse pole figure (IPF-Z) image of the critical transition zone between the top layer and bulk was captured of cube 2.5 and presented in Figure 27.

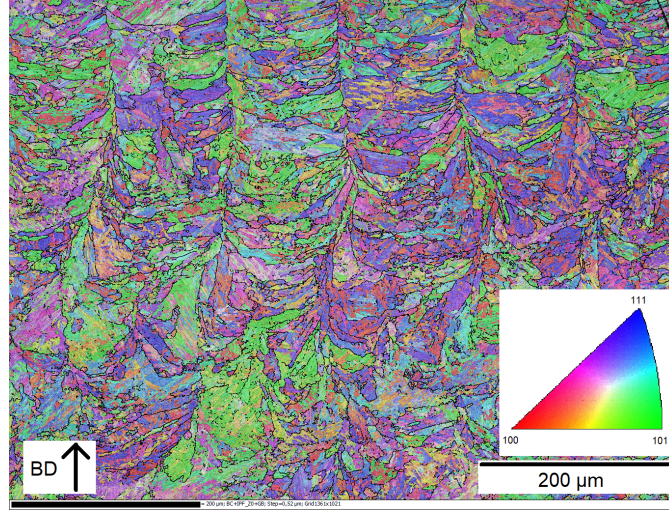


Figure 27: EBSD image capturing the microstructure transition from the top layer to the bulk of cube 2.5 showing the grain boundaries and the crystallographic orientations. The build direction (BD) is shown.

Figure 27 shows a anisotropic columnar microstructure at the top of the image which is the result of the final melt pools solidification. Below the middle of the image, the microstructure changes into a isotropic behaviour which demonstrates the affect of the heat treatment. EBSD was then performed in the top layer and the bulk of cube 2.5 separately to quantify the present phases, the results are presented in Table 4.

Table 4: Results of the EBSD analysis of the top layer and bulk using phase contrast to distinguish different crystal structures.

	Top layer	Bulk
BCC	99.97%	99.01%
FCC	0.03%	0.9%

Table 4 suggest the presence of BCC in the sample which is an interpretation of the EBSD software. The main crystal structure is martensitic BCT which is evident knowing the material composition, production process and by studying the LOM images in Figure 26. Table 4 also shows how a solid phase transition occurs due to the in situ heat treatment as more FCC austenite assemble in the bulk. Note that the sum of the percentages in the bulk analysis does not equal 100%, the main reason for this is the hit rate of the analysis.

4.4 Hardness

The hardness result from the bulk profiles (normalised) are presented in Figure 28. The parameter sets does not have the same amount of data points due to the difference in height of the cubes. It is apparent that all cubes are within 5%

difference from the hardness of the reference cube 1.1 which would indicate that all cubes have equivalent bulk microstructure which seems likely when also studying Figure 26.

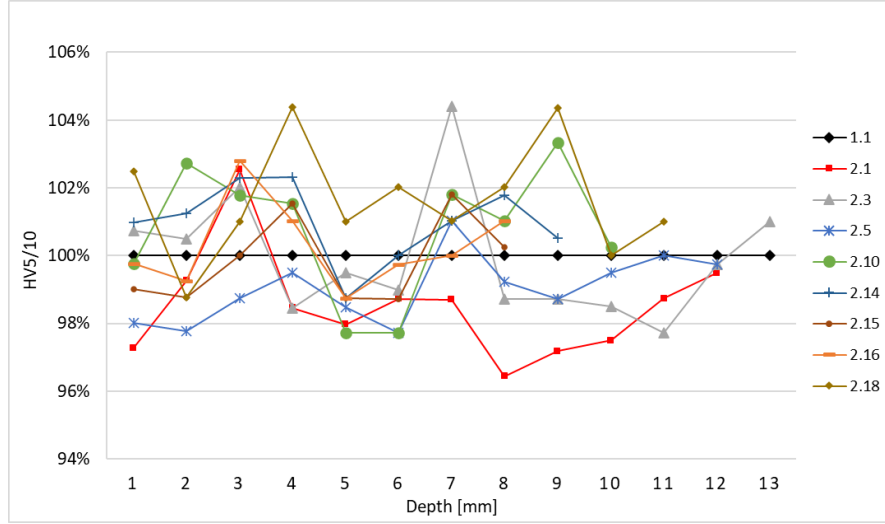


Figure 28: Hardness result of the bulk profiles normalised to the reference cube 1.1. The depth is measured from the top surface of the cube.

The hardness result from the surface profiles (normalised), provided in Figure 29, show a distinctive difference in the first 0.4 mm beneath the surface. All cubes printed in the 2nd iteration have a higher surface hardness than cube 1.1 has. Studying the microstructure in Figure 26 it is clear that the top layer is deeper for cubes of the 2nd iteration, compared to the reference cube 1.1, and that the indentation sites are located in that top layer.

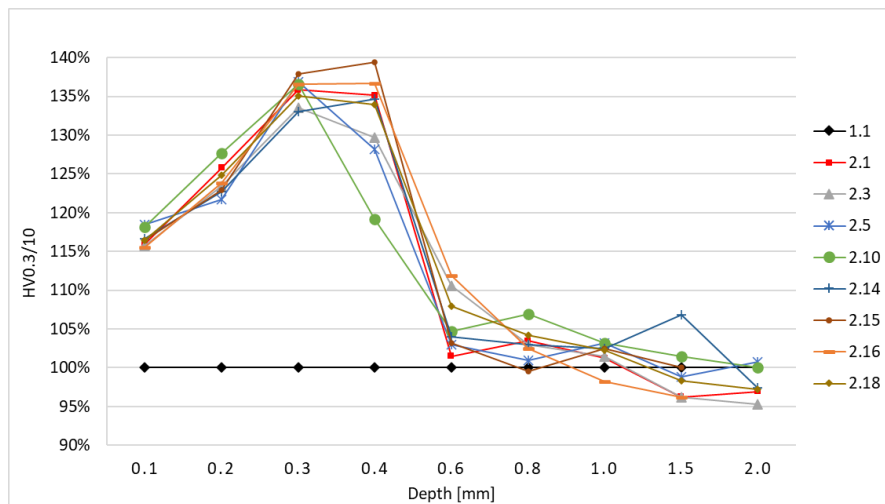


Figure 29: Hardness result of the surface profiles normalised to the reference cube 1.1. The depth is measured from the top surface of the cube. The indentations are visible in Figure 26.

4.5 Mechanical testing

Tensile testing result graphs are presented in Figure 30 for the two parameter sets 2.5 and 2.18. The different test plane orientations are presented with different colors, red for XY (standing) and blue for XZ (lying). Each orientation was tested six times, however two 2.5 lying tensile rods were machined faulty resulting in a missing- and a outlier result. The machine was unreliable while calculating the elongation which were measured by hand instead.

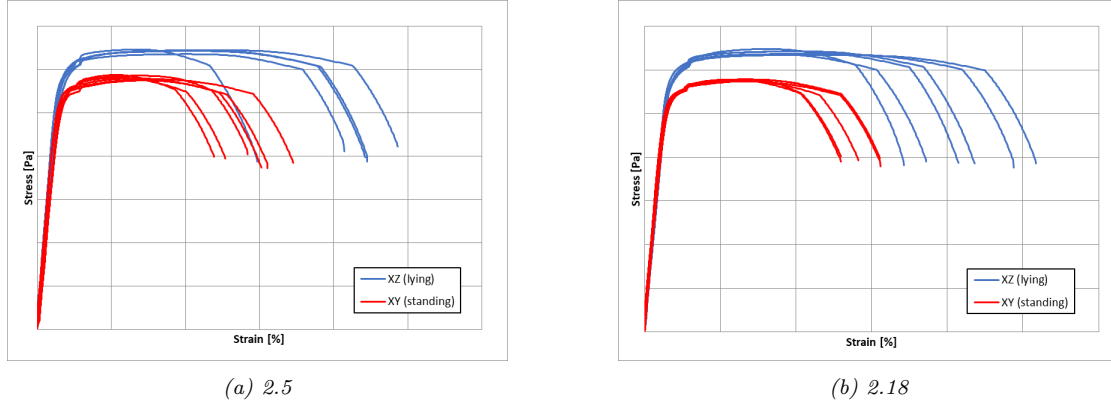


Figure 30: Results from tensile tests. The tensile test curves clearly group in two families depending on the build direction. Lying specimens perform better for both parameter sets.

The resulting data is presented in Table 5 which show how results compare to reference data of samples analysed prior to this project using the 1.1 parameter set. The standard deviation is also compared to the reference data.

Table 5: Results of the mechanical tests, normalised to parameter set 1.1. All values are averages from the experimental results. $R_{p0.2}$ is the yield strength, R_m is the tensile strength, A_5 is the elongation and E represents the impact toughness.

Sample	Test plane	$R_{p0.2}$ [%]	R_m [%]	A_5 [%]	E [%]
2.5	XZ (lying)	95 ± 2	99 ± 1	104 ± 8	68 ± 13
	XY (standing)	94 ± 1	92 ± 1	79 ± 3	48 ± 7
2.18	XZ (lying)	95 ± 1	98 ± 1	107 ± 8	53 ± 9
	XY (standing)	93 ± 0	91 ± 0	81 ± 5	38 ± 6

Figure 30 and Table 5 show that $R_{p0.2}$, R_m , A_5 and E are higher of all the lying samples. Only the elongation of the lying samples improve upon the reference. No impact test is close to matching the reference data.

5 Discussion

The porosity analysis of the 1st printing iteration, Figure 22, had a large variety of results including the nine cubes that were forcefully stopped due to spattering. The parameter sets were constructed in a way to enable comparisons, Figure 15, while increasing the layer thickness, laser power and build rate, but the results was not fully as expected. Most studies develop the operation window while maintaining the same layer thickness, however Sheuan Jason Ten et al. [25] proved that the relative density and material properties could be preserved using the same energy density for different layer thicknesses which the 1st iteration results contradict.

The intensified laser power likely transitioned the melt mode from conduction to keyhole mode with deeper melt pools. Without simultaneously increasing the layer thickness excessive keyhole pores was formed implying a very unstable melt pool. This is similar to the results from Scipioni et al. [21] which, though only performing single track experiments, showed how the stability of the melt pool was affected by a increasing laser power. When the layer thickness was doubled the trend was reversed and keyhole pores were instead diminished as the laser power increased, attributing the complexity of the process. When the layer thickness was tripled only one cube finished printing. The top surface of that cube showed strong signs of balling which could be the reason for its large lack of fusion pores.

The 2nd printing iteration focused on finding a operating window while doubling the layer thickness. Almost all cubes successfully achieved a relative density above 99.95% while having increased the build rate by at least 80%, Figure 20 and 24. A theoretical operating window is presented in Figures 31 which include all finished cubes of the 2nd iteration. Cube 2.3 show increased keyhole porosity which reflect the simplified operation window proposed by Ahmed et al. [7], shown in Figure 13. Cube 2.5 performed the best results indicating that the complete operating window extends further to the top-right than illustrated in Figure 31.

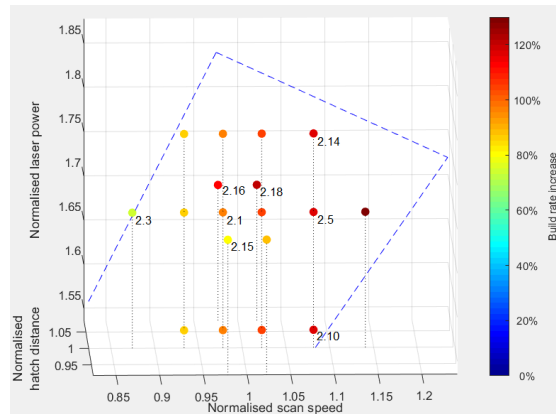


Figure 31: Theoretical operating window encapsulating the finished experimental parameter sets of the 2nd iteration.

Comparing different samples of the 2nd iteration to the reference, the bulk microstructure visually appear to be similar, Figure 26 which the hardness results support, Figure 28. However during mechanical testing the material reacts differently, Table 5. At higher resolution the curtain pattern show some differences, probably due to the in situ heat treatment. Compared to the reference, cubes of the 2nd iteration appear to preserve more pristine martensitic microstructure in the bulk which, due to its brittle nature, could explain the lower impact toughness.

5.1 Future work

To further develop parameter sets a deeper understanding of how the melt pool, solidification and in situ heat treatment influence the resulting microstructure. The EBSD analysis could both show and measure the transition between pristine and heat treated martensite, Figure 27 and Table 4, however no comparisons to the reference was performed during this study. It is possible that the differences of the curtain pattern contains more clues that will help differentiate the reference and tested samples.

To achieve even higher build rates new attempts should be made to increase the layer thickness as many studies have shown it is possible. A possibility to make fast progression could be to use single track experiments and from there determine if a parameter set is promising enough to develop. As the results of the 2nd iteration provide a wide operating window it should be possible to transverse some of those parameter sets as the incline of layer thickness is smaller than the initial trial. It is also possible to further develop the operating window presented in Figure 31.

6 Conclusion

The aim of this study is to increase the build rate of SSAB TS1 steel powder in the L-PBF process. This can be accomplished by tuning the most important process parameters; laser power, scan speed, hatch distance and layer thickness. A operating window producing a relative density above 99.95% was found that simultaneously increased the build rate by at least 80%. The most successful result increased the build rate by 116% while largely maintaining desired material properties.

Acknowledgements

I would like to offer my sincere gratitude to my supervisors Ulrika Fager and Gunnar Broberg for creating this project, allowing me to partake in it and guiding me along the way. Their expertise and encouragement definitely helped me to complete this thesis.

I am grateful to SSAB for providing me with the opportunity to conduct my research and for all of the resources and support they provided. I would also like to extend my heartfelt appreciation to all the participants from SSAB who dedicated their time and contributed to my study. Additionally, I would like to offer a special acknowledgment to Mehreen Baig, Hugo Wärner and Teodor Haglund for their dedicated assistance and for making my experience at SSAB even more enjoyable.

I would like to thank my subject reviewer Urban Wiklund and examiner Lena Klintberg for their understanding and encouraging words which helped me finalise this thesis.

Five years at Uppsala University have passed and I could not be more happy and proud of my journey. To all my friends, to all my family. Thank you.

References

- [1] SSAB marketing. Ssab in brief, 2023. <https://www.ssab.com/en/company/about-ssab/ssab-in-brief/vision-and-values> Accessed on 28 Jun 2023.
- [2] Mohsen Attaran. The rise of 3-d printing: The advantages of additive manufacturing over traditional manufacturing. *Business Horizons*, 60(5):677–688, 2017.
- [3] Shahriar Afkhami, Mohammad Dabiri, Heidi Piili, and Timo Björk. Effects of manufacturing parameters and mechanical post-processing on stainless steel 316l processed by laser powder bed fusion. *Materials Science and Engineering: A*, 802:140660, 2021.
- [4] Gao Huang, Kaiwen Wei, Jinfeng Deng, Mengna Liu, and Xiaoyan Zeng. High-power laser powder bed fusion of 316l stainless steel: Defects, microstructure, and mechanical properties. *Journal of Manufacturing Processes*, 83:235–245, 2022.
- [5] Shubhavardhan Ramadurga Narasimharaju, Wenhan Zeng, Tian Long See, Zicheng Zhu, Paul Scott, Xiangqian Jiang, and Shan Lou. A comprehensive review on laser powder bed fusion of steels: Processing, microstructure, defects and control methods, mechanical properties, current challenges and future trends. *Journal of Manufacturing Processes*, 75:375–414, 2022.
- [6] Faham Tahmasebinia, Amir Abbas Jabbari, and Krzysztof Skrzypkowski. The application of finite element simulation and 3d printing in structural design within construction industry 4.0. *Applied Sciences*, 13(6), 2023.
- [7] N. Ahmed, I. Barsoum, G. Haidemenopoulos, and R.K. Abu Al-Rub. Process parameter selection and optimization of laser powder bed fusion for 316l stainless steel: A review. *Journal of Manufacturing Processes*, 75:415–434, 2022.
- [8] William Hearn. *Development of Structural Steels for Powder Bed Fusion – Laser Beam*. PhD thesis, CHALMERS UNIVERSITY OF TECHNOLOGY, 2023.
- [9] Aiden A. Martin, Nicholas P. Calta, Saad A. Khairallah, Jenny Wang, Phillip J. Depond, Anthony Y. Fong, Vivek Thampy, Gabe M. Guss, Andrew M. Kiss, Kevin H. Stone, Christopher J. Tassone, Johanna Nelson Weker, Michael F. Toney, Tony van Buuren, and Manyalibo J. Matthews. Dynamics of pore formation during laser powder bed fusion additive manufacturing. *Nature Communications*, 10(1):1987, Apr 2019.
- [10] Carsten Engel. Selective laser melting versus electron beam melting, 2014. <https://www.slideshare.net/carstenengel/>

- [11] Sohini Chowdhury, N. Yadaiah, Chander Prakash, Seeram Ramakrishna, Saurav Dixit, Lovi Raj Gupta, and Dharam Buddhi. Laser powder bed fusion: a state-of-the-art review of the technology, materials, properties & defects, and numerical modelling. *Journal of Materials Research and Technology*, 20:2109–2172, 2022.
- [12] S. Sun, M. Brandt, and M. Easton. 2 - powder bed fusion processes: An overview. In Milan Brandt, editor, *Laser Additive Manufacturing*, Woodhead Publishing Series in Electronic and Optical Materials, pages 55–77. Woodhead Publishing, 2017.
- [13] Microtrac Retch GmbH. *Software Guide Dimensions software CAMSIZER X2*, 12 2020. Version 0000.
- [14] Matt Baumber. Size distribution chart, 2020. <https://www.quadro-mpt.com/news-and-events/the-importance-of-particle-size-distribution-in-pharmaceuticals> Accessed on 7 Jun 2023.
- [15] Mostafa Yakout, M.A. Elbestawi, and Stephen C. Veldhuis. Density and mechanical properties in selective laser melting of invar 36 and stainless steel 316l. *Journal of Materials Processing Technology*, 266:397–420, 2019.
- [16] Gao Huang, Kaiwen Wei, and Xiaoyan Zeng. Microstructure and mechanical properties of h13 tool steel fabricated by high power laser powder bed fusion. *Materials Science and Engineering: A*, 858:144154, 2022.
- [17] Claudia Schwerz, Fiona Schulz, Elanghovan Natesan, and Lars Nyborg. Increasing productivity of laser powder bed fusion manufactured hastelloy x through modification of process parameters. *Journal of Manufacturing Processes*, 78:231–241, 2022.
- [18] Hugo Roirand, Benoit Malard, Anis Hor, and Nicolas Saintier. Effect of laser scan pattern in laser powder bed fusion process: The case of 316l stainless steel. *Procedia Structural Integrity*, 38:149–158, 2022. Fatigue Design 2021, International Conference Proceedings, 9th Edition.
- [19] Yude Liu, Meng Zhang, Wentian Shi, Yingyi Ma, and Jin Yang. Study on performance optimization of 316l stainless steel parts by high-efficiency selective laser melting. *Optics & Laser Technology*, 138:106872, 2021.
- [20] Materialise NV. *SLM Build Processor User Manual*, 5 2019. Rev. 05-2019.
- [21] Umberto Scipioni Bertoli, Alexander J. Wolfer, Manyalibo J. Matthews, Jean-Pierre R. Delplanque, and Julie M. Schoenung. On the limitations of volumet-

- ric energy density as a design parameter for selective laser melting. *Materials & Design*, 113:331–340, 2017.
- [22] Zhongji Sun, Xipeng Tan, Shu Beng Tor, and Wai Yee Yeong. Selective laser melting of stainless steel 316l with low porosity and high build rates. *Materials & Design*, 104:197–204, 2016.
 - [23] Shuo Wang, Yude Liu, Wentian Shi, Bin Qi, Jin Yang, Feifei Zhang, Dong Han, and Yingyi Ma. Research on high layer thickness fabricated of 316l by selective laser melting. *Materials*, 10(9), 2017.
 - [24] Wentian Shi, Peng Wang, Yude Liu, Yanjun Hou, and Guoliang Han. Properties of 316l formed by a 400w power laser selective laser melting with 250 μ m layer thickness. *Powder Technology*, 360:151–164, 2020.
 - [25] Jyi Sheuan Jason Ten, Fern Lan Ng, Hang Li Seet, and Mui Ling Sharon Nai. Method to maximize the productivity of laser powder bed fusion systems through dimensionless parameters. *Journal of Laser Applications*, 34(1), 01 2022. 012016.
 - [26] Sagar Patel and Mihaela Vlasea. Melting modes in laser powder bed fusion. *Materialia*, 9:100591, 2020.
 - [27] Wakshum M. Tucho, Vidar H. Lysne, Håkon Austbø, Atle Sjolyst-Kverneland, and Vidar Hansen. Investigation of effects of process parameters on microstructure and hardness of slm manufactured ss316l. *Journal of Alloys and Compounds*, 740:910–925, 2018.
 - [28] E. Liverani, S. Toschi, L. Ceschini, and A. Fortunato. Effect of selective laser melting (slm) process parameters on microstructure and mechanical properties of 316l austenitic stainless steel. *Journal of Materials Processing Technology*, 249:255–263, 2017.
 - [29] Yuze Huang, Tristan G. Fleming, Samuel J. Clark, Sebastian Marussi, Kamel Fezzaa, Jeyan Thiyagalingam, Chu Lun Alex Leung, and Peter D. Lee. Key-hole fluctuation and pore formation mechanisms during laser powder bed fusion additive manufacturing. *Nature Communications*, 13(1):1170, Mar 2022.
 - [30] Subin Shrestha and Kevin Chou. Formation of keyhole and lack of fusion pores during the laser powder bed fusion process. *Manufacturing Letters*, 32:19–23, 2022.
 - [31] Wen Hao Kan, Louis Ngai Sam Chiu, Chao Voon Samuel Lim, Yuman Zhu, Yang Tian, Derui Jiang, and Aijun Huang. A critical review on the effects of process-induced porosity on the mechanical properties of alloys fabricated by laser powder bed fusion. *Journal of Materials Science*, 57(21):9818–9865, Jun 2022.

- [32] Bi Zhang, Yongtao Li, and Qian Bai. Defect formation mechanisms in selective laser melting: A review. *Chinese Journal of Mechanical Engineering*, 30(3):515–527, May 2017.
- [33] Zheng Li, Hao Li, Jie Yin, Yan Li, Zhenguo Nie, Xiangyou Li, Deyong You, Kai Guan, Wei Duan, Longchao Cao, Dengzhi Wang, Linda Ke, Yang Liu, Ping Zhao, Lin Wang, Kunpeng Zhu, Zhengwen Zhang, Liang Gao, and Liang Hao. A review of spatter in laser powder bed fusion additive manufacturing: In situ detection, generation, effects, and countermeasures. *Micromachines*, 13(8), 2022.
- [34] Claudia Schwerz, Ahmad Raza, Xiangyu Lei, Lars Nyborg, Eduard Hryha, and Håkan Wirdelius. In-situ detection of redeposited spatter and its influence on the formation of internal flaws in laser powder bed fusion. *Additive Manufacturing*, 47:102370, 2021.
- [35] M. Gao, Yosuke Kawahito, and Shogo Kajii. Observation & understanding in laser welding of pure titanium at subatmospheric pressure. *Optics Express*, 25:13539, 06 2017.
- [36] Chinnapat Panwisawas, Yuanbo T. Tang, and Roger C. Reed. Metal 3d printing as a disruptive technology for superalloys. *Nature Communications*, 11(1):2327, May 2020.
- [37] Viktor Lindström, Giandomenico Lupo, Jian Yang, Vladyslav Turlo, and Christian Leinenbach. A simple scaling model for balling defect formation during laser powder bed fusion. *Additive Manufacturing*, 63:103431, 2023.
- [38] Wakshum M. Tucho, Priscille Cuvillier, Atle Sjolyst-Kverneland, and Vidar Hansen. Microstructure and hardness studies of inconel 718 manufactured by selective laser melting before and after solution heat treatment. *Materials Science and Engineering: A*, 689:220–232, 2017.
- [39] Peiying Bian, Jing Shi, Yang Liu, and Yanxiang Xie. Influence of laser power and scanning strategy on residual stress distribution in additively manufactured 316l steel. *Optics & Laser Technology*, 132:106477, 2020.
- [40] nanoScience Instruments. Scanning electron microscopy, 2023. <https://www.nanoscience.com/techniques/scanning-electron-microscopy/> Accessed on 28 Jun 2023.
- [41] Oxford instruments nanoanalysis. Electron backscatter diffraction - ebsd, 2023. <https://nano.oxinst.com/products/ebsd/> Accessed on 28 Jun 2023.
- [42] Zwick/Roell. Tensile test, 2023. <https://www.zwickroell.com/industries/materials-testing/tensile-test/> Accessed on 21 Jun 2023.
- [43] Zwick/Roell. Impact test, 2023. <https://www.zwickroell.com/industries/materials-testing/impact-test/> Accessed on 21 Jun 2023.

- [44] Ho-Jin Lee. Effects of the energy density on pores, hardness, surface roughness, and tensile characteristics of deposited astm 316l specimens with powder-bed fusion process. *Materials*, 15(19), 2022.
- [45] Struers. Grinding and polishing consumables, 2023. <https://www.struers.com/en/Products/Grinding-and-Polishing> Accessed on 21 Jun 2023.

Appendix

Process parameters

Table 6: 1st iteration of parameter set, normalised to the reference parameter set 1.1. The labels are as follows: laser power P , scan speed ν , hatch distance h , layer thickness t , energy density E_d (calculated using equation 4) and build rate b (calculated using equation 3).

Name	P	ν	h	t	E_d	b
1.1	1.00	1.00	1.00	1.00	1.00	1.00
1.2	1.16	1.20	1.00	1.00	0.96	1.20
1.3	1.29	1.36	1.00	1.00	0.95	1.36
1.4	1.42	1.56	1.00	1.00	0.91	1.56
1.5	1.56	1.75	1.00	1.00	0.89	1.75
1.6	1.69	1.96	1.00	1.00	0.86	1.96
1.7	1.00	0.50	1.00	2.00	0.99	1.01
1.8	1.16	0.60	1.00	2.00	0.96	1.20
1.9	1.29	0.68	1.00	2.00	0.95	1.36
1.10	1.42	0.78	1.00	2.00	0.91	1.56
1.11	1.56	0.87	1.00	2.00	0.89	1.75
1.12	1.69	0.98	1.00	2.00	0.86	1.96
1.13	1.00	0.33	1.00	3.00	1.00	1.00
1.14	1.16	0.39	1.00	3.00	0.98	1.18
1.15	1.29	0.45	1.00	3.00	0.95	1.36
1.16	1.42	0.52	1.00	3.00	0.91	1.56
1.17	1.56	0.59	1.00	3.00	0.89	1.76
1.18	1.69	0.65	1.00	3.00	0.86	1.96

Table 7: 2nd iteration of parameter set, normalised to the reference parameter set 1.1. The labels are as follows: laser power P , scan speed ν , hatch distance h , layer thickness t , energy density E_d (calculated using equation 4) and build rate b (calculated using equation 3).

Name	P	ν	h	t	E_d	b
2.1	1.69	0.98	1.00	2.00	0.86	1.96
2.2	1.69	0.93	1.00	2.00	0.90	1.87
2.3	1.69	0.87	1.00	2.00	0.97	1.75
2.4	1.69	1.02	1.00	2.00	0.83	2.04
2.5	1.69	1.08	1.00	2.00	0.78	2.16
2.6	1.69	1.14	1.00	2.00	0.74	2.28
2.7	1.56	0.98	1.00	2.00	0.80	1.96
2.8	1.56	0.93	1.00	2.00	0.83	1.87
2.9	1.56	1.02	1.00	2.00	0.76	2.04
2.10	1.56	1.08	1.00	2.00	0.72	2.16
2.11	1.78	0.98	1.00	2.00	0.91	1.96
2.12	1.78	0.93	1.00	2.00	0.95	1.87
2.13	1.78	1.02	1.00	2.00	0.87	2.04
2.14	1.78	1.08	1.00	2.00	0.82	2.16
2.15	1.69	0.98	0.92	2.00	0.94	1.79
2.16	1.69	0.98	1.08	2.00	0.80	2.12
2.17	1.69	1.02	0.92	2.00	0.90	1.87
2.18	1.69	1.02	1.08	2.00	0.76	2.21